

Journal of Biomedical Optics

SPIEDigitalLibrary.org/jbo

Continuous sensing of tumor-targeted molecular probes with a vertical cavity surface emitting laser-based biosensor

Natesh Parashurama
Thomas D. O'Sullivan
Adam De La Zerda
Pascale El Kalassi
Seongjae Cho
Hongguang Liu
Robert Teed
Hart Levy
Jarrett Rosenberg
Zhen Cheng
Ofer Levi
James S. Harris
Sanjiv S. Gambhir

Continuous sensing of tumor-targeted molecular probes with a vertical cavity surface emitting laser-based biosensor

Natesh Parashurama,^{a*} Thomas D. O'Sullivan,^{b,*†} Adam De La Zerda,^{a,b} Pascale El Kalassi,^b Seongjae Cho,^b Hongguang Liu,^a Robert Teed,^{a,g} Hart Levy,^{c,d} Jarrett Rosenberg,^a Zhen Cheng,^a Ofer Levi,^{c,d} James S. Harris,^{b,f} and Sanjiv S. Gambhir^{a,e,f,g}

^aStanford University, Molecular Imaging Program at Stanford (MIPS), Division of Nuclear Medicine, Department of Radiology, James H. Clark Center, 318 Campus Drive, E153, Stanford, California 94305

^bStanford University, Department of Electrical Engineering, 475 Via Ortega, Stanford, California 94305

^cUniversity of Toronto, Institute of Biomaterials and Biomedical Engineering, Rosebrugh Building, 164 College Street, Room 407, Toronto, Ontario M5S 3G9, Canada

^dUniversity of Toronto, The Edward S. Rogers Sr. Department of Electrical and Computer Engineering, 10 King's College Road, Toronto, Ontario M5S 3G4, Canada

^eStanford University, Department of Bioengineering, 318 Campus Drive, Stanford, California 94305

^fStanford University, Department of Materials Science and Engineering, 496 Lomita Mall, Stanford, California 94305

^gStanford University, Canary Center for Early Detection of Cancer, 1501 South California Avenue, Palo Alto, California 94304

Abstract. Molecular optical imaging is a widespread technique for interrogating molecular events in living subjects. However, current approaches preclude long-term, continuous measurements in awake, mobile subjects, a strategy crucial in several medical conditions. Consequently, we designed a novel, lightweight miniature biosensor for *in vivo* continuous optical sensing. The biosensor contains an enclosed vertical-cavity surface-emitting semiconductor laser and an adjacent pair of near-infrared optically filtered detectors. We employed two sensors (dual sensing) to simultaneously interrogate normal and diseased tumor sites. Having established the sensors are precise with phantom and *in vivo* studies, we performed dual, continuous sensing in tumor (human glioblastoma cells) bearing mice using the targeted molecular probe cRGD-Cy5.5, which targets $\alpha_v\beta_3$ cell surface integrins in both tumor neovasculature and tumor. The sensors capture the dynamic time-activity curve of the targeted molecular probe. The average tumor to background ratio after signal calibration for cRGD-Cy5.5 injection is approximately 2.43 ± 0.95 at 1 h and 3.64 ± 1.38 at 2 h ($N = 5$ mice), consistent with data obtained with a cooled charge coupled device camera. We conclude that our novel, portable, precise biosensor can be used to evaluate both kinetics and steady state levels of molecular probes in various disease applications. © 2012 Society of Photo-Optical Instrumentation Engineers (SPIE). [DOI: [10.1117/1.JBO.17.11.117004](https://doi.org/10.1117/1.JBO.17.11.117004)]

Keywords: molecular imaging; vertical-cavity surface-emitting laser; noninvasive sensing; angiogenesis; continuous sensing; semiconductor sensors; molecular probes; molecular probe kinetics.

Paper 12443 received Jul. 12, 2012; revised manuscript received Sep. 24, 2012; accepted for publication Sep. 25, 2012.; published online Nov. 2, 2012.

1 Introduction

Molecular imaging of living subjects (MI), in contrast to anatomical or physiological imaging, visualizes molecular probes that delineate biological mechanisms,¹ detect early disease,¹ lead to new diagnostic tests and diagnostic pathways,² and assist in both drug development³ and therapeutic monitoring.⁴ Near-infrared (650 to 1000 nm) optical fluorescence imaging, in particular, benefits from low tissue optical absorption and low tissue autofluorescence leading to increased depth resolution and high sensitivity. Owing to this, optical imaging of a wide range of crucial biological processes such as stem cell homing⁵ and growth,⁶ host infection and virus-host interactions,⁷ arterial plaque assessment,⁸ biological oxidation-reduction reactions,⁹ and tumor angiogenesis¹⁰ are all areas of significant research

activity. Furthermore, optical imaging does not employ ionizing radiation, requires relatively low-cost instrumentation and is capable of characterizing a wide range of spatial scales (microscopic to whole-body). Optical contrast is provided endogenously (e.g., blood), using near-infrared fluorescent proteins,¹¹ or with administration of exogenous probes, including novel small molecule labeled probes, activatable probes,¹² biopharmaceutical labeled probes,¹³ and nanoparticle-based probes.¹⁴ While optical MI techniques have advanced biological research considerably, some limitations still remain. Constraints are imposed by the use of broadband excitation sources and filters, bulky detector systems, and light-tight chambers. Living subjects imaged in these systems commonly need to be immobilized, anesthetized, and repeatedly positioned. Changes in distance and orientation between the detector and subject may adversely affect spatial resolution and sensitivity. Continuous long-term (days to weeks) imaging is impossible, as keeping the animal under anesthesia and/or in a light-tight enclosure strains nutritional requirements and may alter physiological

*These authors contributed equally to this work.

†Present address: Beckman Laser Institute, University of California, Irvine, California 92612

Address all correspondence to: Sanjiv Sam Gambhir; Stanford University, Molecular Imaging Program at Stanford (MIPS), Division of Nuclear Medicine, Department of Radiology, James H. Clark Center, 318 Campus Drive, E153, Stanford, California 94305. E-mail: sgambhir@stanford.edu

states. To address these issues, we and others have developed miniature, minimally invasive *in vivo* molecular sensors that can be implanted or worn by the subject continuously.

An optical sensor enables continuous, long-term sensing of targeted probe dynamics in freely moving subjects at potentially high temporal resolution. Continuous optical sensing with a miniature design has been pursued with complementary metal oxide semiconductor (CMOS) detector arrays,¹⁵⁻¹⁷ fiber optics,¹⁸ and integrated III-V semiconductor devices.¹⁹ We have developed a miniature semiconductor-based fluorescent sensor containing a vertical-cavity surface-emitting laser (VCSEL), gallium arsenide PIN diode, and a fluorescence emission filter. The sensor is potentially applicable to *in vitro* diagnostics,²⁰ *in vivo* exogenously induced fluorescence,¹⁹ and deep tissue fluorescence via implantation.²¹ The sensors have a high sensitivity (5 nM *in vitro*, and autofluorescence-limited to 50 nM *in vivo*),¹⁹ and because they are produced with standard semiconductor fabrication techniques, the sensors are scalable for both larger pixel formats and lower-cost manufacturing. Thus VCSEL-based biosensors are a good candidate for *in vivo* continuous molecular sensing.

An important aspect of molecular sensing is determining levels of a molecular target within any arbitrary organ system. In theory, this could be accomplished by sensing the levels of an injected molecular probe, which accumulates and generates signal proportional to a molecular target of interest. An example of a candidate system is tumor vasculature in the setting of neoangiogenesis, or newly formed vasculature, which occurs during tumorigenesis. Neoangiogenesis is linked to chemotherapeutic transport, tumor oxygenation, nutrient supply, and tumor growth.²² Importantly, targeting and imaging neoangiogenesis is an active area of investigation in molecular imaging.²³⁻²⁵ Because tumor vasculature represents a focused spatial location for immediate (post treatment) and long-term (during tumor recurrence) dynamics, it is a relevant platform for biosensing. A commonly used molecular probe for neoangiogenesis is the RGD peptide, which, depending on its configuration, binds with nanomolar affinity to the $\alpha_V\beta_3$ integrin.^{26,27} These integrins are highly up-regulated on both neoangiogenic and activated endothelial cells,²⁸ on the surface of specific tumor types, and on activated macrophages involved in inflammation.²⁹ They have been targeted with RGD containing molecular imaging probes and imaged using positron emission tomography (PET),³⁰ magnetic resonance imaging (MRI),³¹ and ultrasound.³² Optical imaging utilizing the RGD probe in preclinical xenograft cancer models has been successfully demonstrated by conjugating RGD or modified RGD with fluorophore,^{26,33,34} and the cyclic RGD peptide conjugated to Cy5.5 (cRGD-Cy5.5) is a well-established optical imaging probe. Overall, these studies demonstrated increased tumor specific and receptor specific binding of cRGD-Cy5.5 with a reported signal-to-background ratio of 1.5 to 4.5, making it an attractive system to investigate using biosensing.

In this study, we aim to use the novel VCSEL-based sensor for continually sensing the molecular probe (cRGD-Cy5.5) within tumors. We characterize the sensor output by performing *in vitro*, tissue-simulating phantom (liquid and solid), and *in vivo* measurements. We establish that the signal from the VCSEL sensor is precise and stable. Finally, we demonstrate the ability to sense levels of a well-established molecule probe, cRGD-Cy5.5, which targets neoangiogenesis tumors in a mouse tumor model, develop simple approaches for sensor calibration,

and demonstrate that a wide range of kinetic differences can be captured. Overall, we provide a framework for establishing quantitative biosensing approaches as a complement to traditional, optical MI.

2 Materials and Methods

2.1 Cell Culture and Tumor Implantation

U87MG cells were cultured in Dulbecco's modified Eagle's medium containing high glucose (Invitrogen, Carlsbad, California), which was supplemented with 10% fetal bovine serum and 1% penicillin-streptomycin. The cells were expanded in tissue culture dishes and kept in a humidified atmosphere of 5% CO₂ at 37°C. The medium was changed every other day. All animal protocols were approved by the Institutional Administrative Panel on Laboratory Animal Care. For tumor implantation, 5 to 10 × 10⁶ cells were mixed in a 1:1 ratio with Matrigel (BD Biosciences) at a total volume of 100 μL and implanted subcutaneously in the hindlimb of adult female nude mice aged six to eight weeks (Charles River). Mice were monitored weekly, and typically after two weeks to one month, the mice were ready for injection of molecular probe and sensing.

2.2 Design of a Miniature Fluorescent Sensor

The miniature fluorescence sensors utilized in these studies consist of an array of five 675-nm VCSEL sources and two gallium arsenide (GaAs) PIN detectors with integrated fluorescence emission filters in a hybrid configuration. The design and fabrication of these sensors, and specifically the integrated detector, have been described previously.³⁵ The lasers are capable of emitting up to 1.5 to 1.7 mW optical power at 675 nm in multimode operation at room temperature with laser line widths less than 0.2 nm full width half maximum (FWHM). The GaAs detectors exhibit dark currents less than 5 pA/mm² for 100 mV bias and quantum efficiencies surpassing 75%.

One laser in each sensor was operated during sensing. The excitation lasers were current driven with a sinusoidal 2 mA (peak-to-peak) waveform on top of an 8 mA DC offset (Keithley Instruments 6221) at 23 Hz resulting in an average optical power of ~0.75 to 1.0 mW. The unbiased detectors were read with a lock-in amplifier (Stanford Research Systems SRS 830) with a 300-ms time constant. We read the two detectors in each sensor, switching between them with an automated switch system (Keithley Instruments 7001 system with 7158 scanner cards). After switching, we delayed current reading by 5 s to allow the signal to settle. Much faster switching is possible by dedicating a separate readout channel to each detector. All the signal lines to and from the instrumentation were protected with a grounded shield. The instrumentation was automatically controlled by a Matlab (Mathworks) program over GPIB interface. Data was obtained in the form of root mean square (RMS) signal and background was subtracted to obtain final value, in picoamps, at each point.

2.3 Field-of-View Determination

The sensor field-of-view was estimated in a tissue-simulation phantom. A 1.15-mm inner diameter (0.20-mm wall thickness) glass capillary tube filled with 50-μM Cy5.5 in PBS was fixed inside a container of liquid phantom formulated with 0.6% Intralipid (Fresenius Kabi, Germany) in distilled water to model

tissue scattering. We neglected tissue absorption component in the phantom because, in the near-infrared³⁶ spectrum, the absorption coefficient is negligible in comparison to the scattering coefficient.³⁷ The scattering coefficient of this phantom was verified using a spatially resolved diffuse reflectance probe. To test field-of-view using the capillary tube filled with fluorophore, the sensor was fixed while the container containing the capillary tube and liquid phantom material was translated on a stage relative to the sensor. We tested signal variation by varying the stage in x , y , and z directions. Signal was corrected for background from excitation leakage as well as excitation backscatter from the phantom, by subtracting this data from the signal in the presence of the Cy5.5 fluorophore. We performed three separate experiments, with two detectors for each experiment. For each experiment, signal was normalized to the maximum signal in that experiment. Data between experiments was presented as mean \pm standard deviation of the normalized signal. We plotted effects of varying depth (Z) as well as varying lateral position and height (Y , Z).

2.4 Tissue Phantom

A flexible, cylindrical silicon phantom, height = 2 cm, diameter = 5 cm, with negligible absorption and uniform scattering was used. Embedded titanium dioxide particles were used to provide uniform scattering properties. Absorption coefficient was $4.15 \times 10^{-13} \text{ cm}^{-1}$ and the reduced scattering coefficient was 5.89 cm^{-1} .

2.5 Imaging with a Cooled CCD Camera

Animal handling was performed in accordance with Stanford University Animal Research Committee guidelines. Mice were gas anesthetized using isoflurane (2% isoflurane in 100% oxygen, 1 L/min) during all injection and imaging procedures. Nude mice were imaged using a cooled charge-coupled device (CCD) camera (Xenogen IVIS29; Xenogen Corp.). Nude mice with either Cy5.5 fluorophore subcutaneously injected, or nude mice bearing U87 tumors injected intravenously (tail vein) with 3 nmol of cRGD-Cy5.5, or cRAD-Cy5.5 fluorophore, were imaged in the CCD camera. The animals were placed prone in a light-tight chamber, and a grayscale reference image was obtained under low-level illumination. Photons emitted from cells implanted in the mice were collected and integrated for 3 min. Images were obtained using Living Image Software version 2.5 (Xenogen Corp.) To quantify the measured light, the average radiance (photons per second per square centimeter per steradian) was obtained over regions of implanted cells as validated previously. During each experiment, acquisition time, distance between CCD and the mouse, and other imaging parameters were kept constant.

2.6 Synthesis of cRGD-Cy5.5, cRAD-Cy5.5 Conjugates

Arg(R)-Gly(G)-Asp(D)-DTyr(y)-Lys(K) (RGDyK) and Arg(R)-Ala(A)-Asp(D)-DTyr(y)-Lys(K) (RADyK) (Peptides International, Inc.) and Cy5.5-NHS (GE Healthcare/Amersham) were used to synthesize conjugates. RGD peptide c(RGDyK), or RAD peptide c(RADyK), (1 μmol) in 0.25 mL of 0.1 mol/L sodium borate ($\text{Na}_2\text{B}_4\text{O}_7$) buffer (pH = 8.5) were mixed with Cy5.5-NHS (1.2 mg, 1.1 μmol) in H_2O (0.25 mL) at 4°C. The reaction vessel was wrapped under

aluminum foil, and the mixture was allowed to warm to room temperature and react for 2 h. The reaction was then quenched by adding 20 μL of 1% TFA. After HPLC purification, the Cy5.5-RGD and Cy5.5-RAD conjugates were redissolved in saline at a concentration of 1 mg/mL, and stored in the dark at -20°C until use. The purified conjugates were characterized by MALDI-TOF MS. Cy5.5-c(RGDyK): $m/z = 1,243.4$ for $[\text{M} + \text{H}]^+$ ($\text{C}_{59}\text{H}_{75}\text{N}_{11}\text{O}_{15}\text{S}_2$, calculated MW = 1242.42); Cy5.5 c(RADyK). The structure of Cy5.5-c(RGDyK), and the HPLC results after synthesis and of Cy5.5-c(RGDyK) and Cy5.5-c(RADyK) were consistent with known values.

2.7 In Vitro and Live Mouse Sensitivity Measurements

Initially, experiments to test *in vitro* and live mouse sensitivity of the sensor were performed as described previously by O'Sullivan et al.¹⁹ Briefly, various concentrations of Cy5.5 (GE Healthcare, Catalog #PA15602) are diluted in 100 μL volumes of H_2O . The fluorescence emission is measured and the background signal subtracted. All experiments are performed in a single clear-bottom plastic well (~ 7 mm diameter) (Stripwell 1 \times 8, Corning Inc. from 96 well plates). For phantom experiments, a tissue phantom, which mimics the scattering properties tissue, was used. For live mouse sensing, two sensors are placed in symmetrical sites bilaterally at the level of the mouse hindlimb. The sensors are in near contact with skin, and after recording a background measurement, 50 μL of subcutaneous fluorophore at varying concentrations, or phosphate buffered saline (PBS), is injected and live mouse sensing is performed. Each measurement was repeated twice for each concentration. Raw data was plotted as signal versus time for each detector. The actual fluorescence signal is determined by subtracting the background signal (due to backscattering and autofluorescence) from the measured photocurrent after probe injection for each detector. After measuring with the integrated sensor, typically 4 h, the mouse was brought to a small animal CCD-based fluorescence imager (IVIS, Caliper Life Sciences, Hopkinton, MA) for comparison with the last signal obtained with the VCSEL. We have verified using time-sequential imaging that the detected fluorescence intensity does not change appreciably in the time elapsed between the sensor measurements and CCD imaging steps (data not shown).

2.8 Sensing of Cy5.5 or cRGD-Cy5.5 After Intravenous Injection

Animal handling was performed in accordance with Stanford University Animal Research Committee guidelines. To perform sensing, mice were anesthetized and placed on a heated stage in a prone position with continuous anesthesia (1% to 2%). Sensors were placed and fixed perpendicular to the tumor and control site, bilaterally, near the hindlimb. Background signal was acquired for anywhere between 5 and 30 min prior to injection. Three nmol of Cy5.5 dye alone, cRGD-Cy5.5, or cRAD-Cy5.5 in a total volume of 50 μL were injected by tail-vein catheter. The rise and decay of signal were measured anywhere between 2 and 4 h. All instrumentation was described as above, and Matlab software (version 7.0) was used to run and acquire continuous data of the detector current.

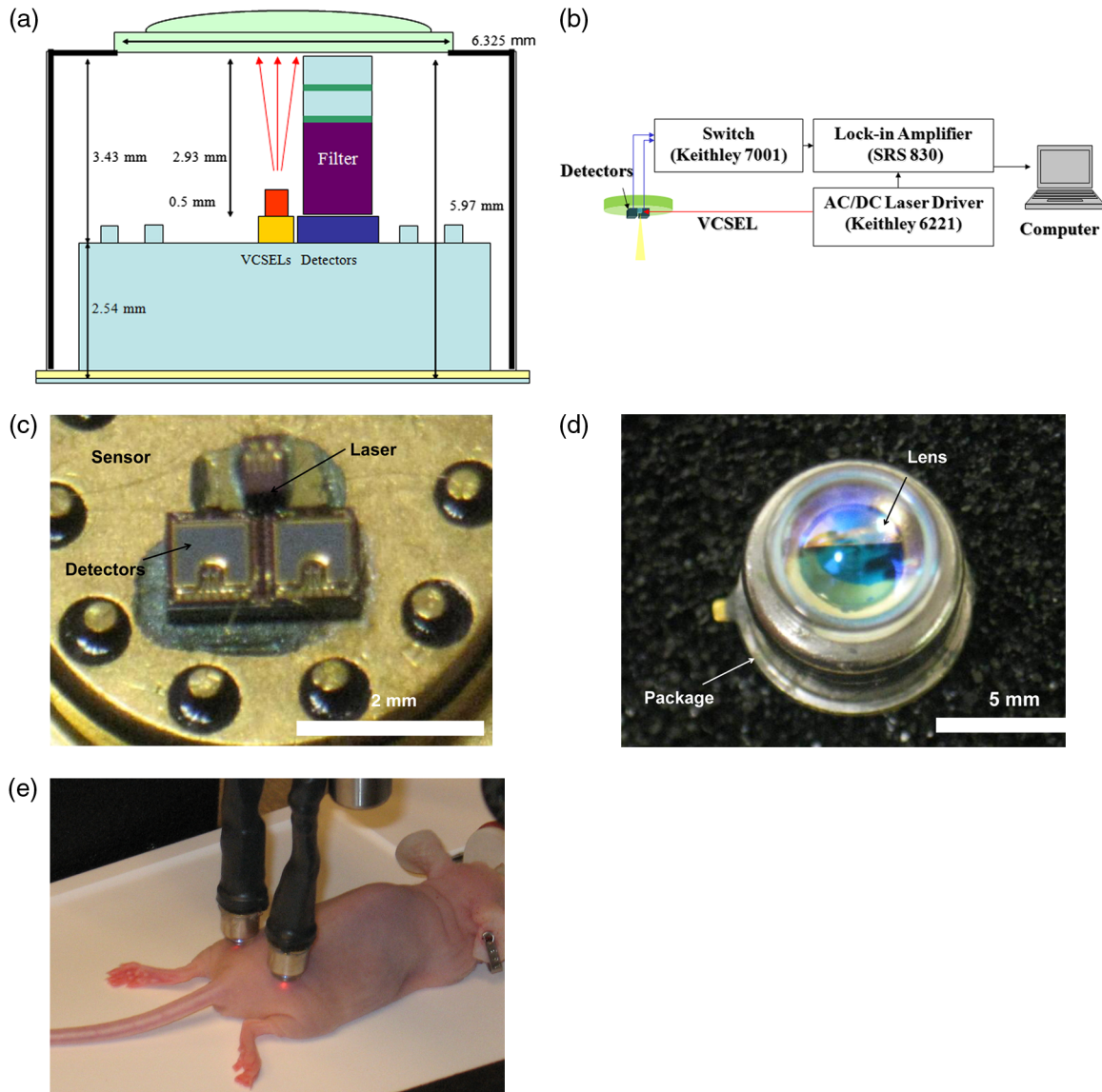


Fig. 1 Experimental system for sensing. (a) Schematic of VCSEL biosensor demonstrating internal dimensions. Each VCSEL biosensor, fabricated from a gallium arsenide (GAs) chip, has one VCSEL, and two detectors (shown as 1 in schematic) with stacked filters on top of the detectors; (b) schematic demonstrating the VCSEL, the detectors, and signal processing system. The laser driver drives the laser. The signal generated is controlled by switching system between detectors, and passes to the lock-in amplifier, which outputs data on computer; (c) image of complete sensor with pins for contacts located circumferentially along perimeter, two horseshoe shaped detectors, and a laser source in the center. Bar = 2 mm; (d) high magnification image of packaged sensor demonstrating lens and metal package. Bar = 5 mm; and (e) experimental setup with vertically oriented sensors nearly in contact on both flanks of anesthetized, nude mice.

2.9 Data Analysis, Curve Fitting, and Statistics

For characterization of sensor, data is expressed in mean \pm standard deviation. For measuring the variation in sensing with time in live mouse studies, the coefficient of variation, the standard deviation divided by the mean, is used. Routine linear fitting was performed on curves of the detector 1 versus detector 2 plot. For comparing the mean and deviation between conditions, a student paired *t*-test with two tails was used.

3 Results

3.1 Experimental System for Sensing

A schematic with internal dimensions of the sensor is shown [Fig. 1(a)]. For fluorescence sensing, excitation light passes

through the collimating lens and illuminates the target, with a spot size of approximately 2 mm. Scattered excitation light and fluorescence emission both pass back through the lens. Light is filtered by the emission filter and passes to the detector, resulting in a current signal. We used a lock-in technique to reduce the electrical noise in the system, as shown in the block diagram of the signal processing and acquisition system [Fig. 1(b)]. A major concern was to identify sources of noise when sensing, and so we chose to include two identically engineered detectors in each sensor to help decouple potential sources of noise, such as movement of sensor or object. The two independent detectors, are called D1 and D2, and each gives rise to a unique signal. A top view of the sensor shows an integrated sensor with two adjacent detectors, a laser located medially is shown [Fig. 1(c)], as is the complete packaged

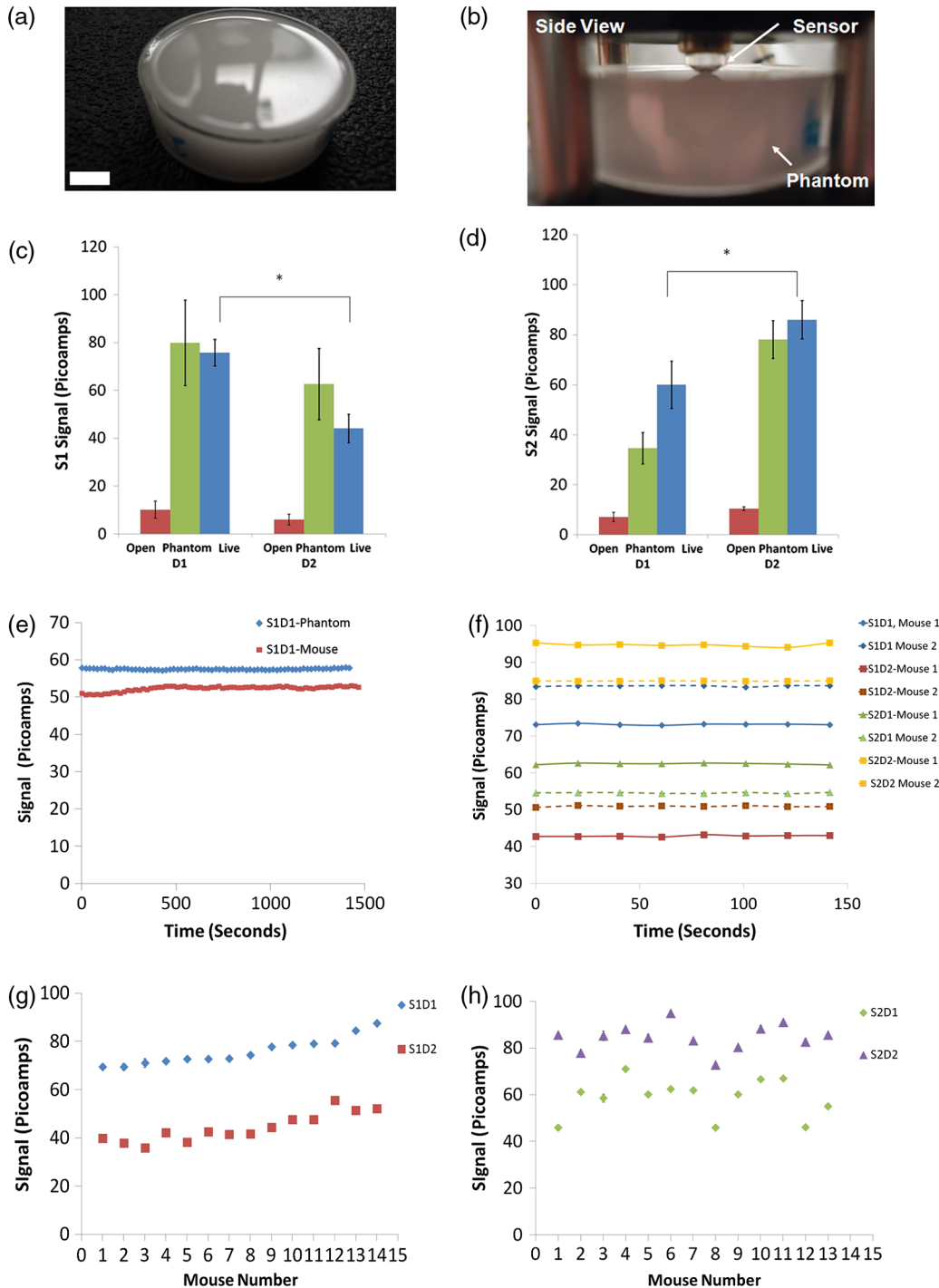


Fig. 2 Determination of repeatability of VCSEL sensor using *in vitro*, phantom, and *in vivo* experiments. (a) Tissue simulating phantom, which mimics scattering and absorption of tissue in the near infrared range. The cylindrical phantom (height = 2 cm, diameter = 5 cm) has negligible absorption and uniform scattering properties. Embedded titanium dioxide particles were used to provide uniform scattering properties. Bar = 1 cm; (b) same phantom in (a) except in close contact with sensor above. Sensor was fixed perpendicularly as shown. Distance between sensor and phantom was 100 μm ; (c) comparison of the repeatability of the S1 sensor between the open, phantom, and live mouse conditions, for the D1 and D2 detectors. For the open condition, no object was present. For the phantom condition, a tissue-stimulating phantom was used. For the live mouse condition, two sensors were placed vertically and directly above each side of the hindlimb region of an anesthetized live mouse. Repeatability for open and phantom conditions was measured by acquiring the average signal over 400 s, after recreating the experimental setup. For the live mouse experiment, the sensor, repeatability was measured by averaging the sensing data over 400 s for several mice. Data represented as mean of signal \pm standard deviation ($N = 15$); (d) same as (c) except S2 sensor data is shown; (e) comparison of the long-term signal stability of the S1 and S2 sensors while sensing the tissue-simulating phantom. Sensing was performed for 3200 s or 1 h, and 1500 s of stable signal is shown here. Absolute signal for S1D1 and S2D1 shown; (f) comparison of the differences in signal between two sensors, each with two different detectors, in two different mice, for the same mouse experiments as in (a). Two mice from the total of 15 are highlighted to demonstrate differences in signal between two mice; (g) same data as in (c–d) except comparison of signal measured for individual mice. Data represented as mean of signal \pm standard deviation and is ordered from lowest signal to highest signal ($N = 15$ mice); and (h) same as (g) except for S2 sensor. Mice are in same order as in (g).

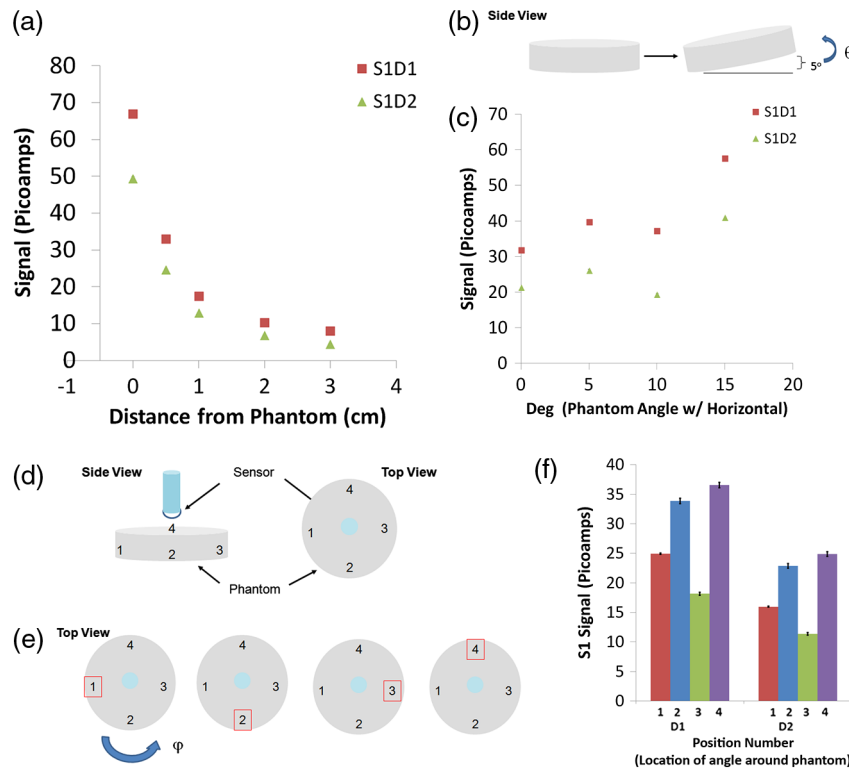


Fig. 3 Determination of positional effects between phantom and sensor on sensor signal. (a) Determination of the effects of distance from phantom on precision of the signal for the S1 sensor. Signal is acquired at the distance between sensor and phantom at 0, 0.5, 1, 2, 3 cm. Signal was acquired every 40 s for 600 s or 10 min at each height. Data presented as the mean of signal \pm standard deviation for a single trial; (b) schematic of experiment in which tissue simulating phantom is angled from 0 to 15 deg compared to horizontal in 5-deg increments as shown. This angle is termed " θ ." Side view of phantom is shown; (c) determination of the effects of angle between phantom and sensor on precision of the signal for the S1 sensor. Signal is acquired at varying angles between phantom and sensor. Angle is created by raising the edge of the phantom at 5 deg, 10 deg, or 15 deg compared to the horizontal. Signal was acquired every 20 s for 600 s or 10 min at each angle. Data presented as the mean of signal \pm standard deviation; (d) schematic in which tissue simulating phantom is labeled at four different positions. Phantom is labeled at four points separated by 90 deg circumferentially. The left diagram demonstrates side view of sensor placed vertically and phantom with four labels. The right diagram demonstrates top view with four positions (1 to 4) labeled; (e) schematic of experiment in which phantom is angled at one dimension and rotated in another dimension. Four schematics of top view of phantom shown, with red square enclosing position number, depicting location of angle. Phantom is angled at 5 deg to horizontal, as in (a). Then the angle is moved about phantom in 90-deg increments counterclockwise, labeled as " ϕ ". At each angle ϕ , the signal is acquired with sensor in a vertical position, directly in contact with phantom; and (f) determination of the effects of location of angle on precision of the signal for the S1 sensor. First, an angle is created by raising the edge of the phantom at 5 deg compared to the horizontal (θ). Then the phantom with an angle is rotated clockwise in cylindrical phantom at four different positions (ϕ). Signal is acquired every 20 s for 600 s or 10 min at each angle. Data presented as the mean of signal \pm standard deviation.

sensor with lens [Fig. 1(d)]. The experimental setup used for dual sensing of a targeted probe *in vivo* is shown [Fig. 1(e)]. A nude mouse was anesthetized and placed in the prone position with abdomen down on a heated stage. Two sensors were fixed vertically and symmetrically in direct proximity to the skin in the mouse's hindlimb region. In terms of positioning the sensor, when the term "direct contact" was used, the lens was placed at a distance of 100 μ m from the object, which was as physically close to the tissue as possible without touching the tissue. The laser excitation light striking the mouse appears red [Fig. 1(e)]. Signal was acquired from both sides of the mouse to obtain a unique baseline measurement in each detector of each sensor, after which subcutaneous or intravenous injection of the fluorescent molecular probe was performed.

3.2 Determination of Precision, Repeatability, and Long-Term Stability of Sensor Using a Phantom and Experiments in Live Mice

We aimed to measure signal precision, repeatability, and stability of the sensor. Here precision is defined as the variation

of signal in comparison to the mean of a series of repeat measurements. Repeatability is defined as the measurements made on the same object after setting up a sensing system, performing measurements, disassembling the setup, reassembling the system, and again performing measurements. Stability is defined as long-term (greater than 20 min) sensing with the same sensor of a fixed object. To do this, we performed experiments using both a solid, silicon tissue-simulating phantom [Fig. 2(a)] as well as mice. The phantom mimics tissue light scattering without absorption or autofluorescence in the NIR range, whereas the mouse exhibits light scattering with a small amount of autofluorescence. We designated the same two sensors to be used for all experiments as "S1" or "S2," each containing two detectors referred to "D1" and "D2." We placed the sensor into direct contact with the phantom or mouse to characterize noise due to back-scattered excitation light [Fig. 2(b)]. Precision ranged from 0.291% to 0.941% for S1 and S2 sensors for open (no phantom), phantom, and live mouse conditions (Table 1, coefficient of variation, CV%, $N = 20$ measurements), and similar results were obtained in several experiments. Repeatability ranged from 9.7% to 23.87% for the phantom condition, and 7.28%

Table 1 Precision of S1 and S2 sensors in open, phantom, and *in vivo* conditions for $N = 20$ measurements.

Configuration	Mean-D1 (pA)	Stdev (pA)	Mean-D2 (pA)	Stdev (pA)	D1 CV%	D2 CV%
S1-open	13.038	0.075	6.628	0.062	0.572	0.941
S1-phantom	101.159	0.341	79.710	0.277	0.291	0.362
S1- <i>in vivo</i>	56.851	0.315	50.653	0.462	0.553	0.911
S2-open	9.825	0.079	11.319	0.087	0.808	0.766
S2-phantom	39.482	0.216	83.612	0.244	0.54	0.38
S2- <i>in vivo</i>	41.830	0.310	68.865	0.574	0.742	0.834

to 14.07% for the live mouse case for both sensors [Fig. 2(c) and 2(d), Table 2, $N = 5$ (open and phantom), $N = 15$ mice, CV%). For signal stability, we measured the signal for 20 min, and in some cases we performed sensing for as long as 60 min [Fig. 2(e), $N = 4$]. We calculated CV% as a measure of variation with time. For the open (no phantom) condition, the CV% was <3.31% for S1D1, and <2.83% for S1D2. For the phantom condition, the CV% was <2.37% for S1D1 and <3.29% for S1D2. For the live mouse condition, the CV% was <2.18% for S1D1 and <3.27% for S1D2 (Table 3, $N = 4$). To illustrate differences in signal between individual mice, we plotted data from both detectors in each sensor in two mice [Fig. 2(f)]. Each detector value changes when comparing the first mouse to the second mouse. We compared the mean values for all mice by plotting the mean \pm SD for both the S1 sensor and the S2 sensor for each mouse [Figs. 2(g) and 2(h), $N = 14$]. The mean values for the S1 sensor were 75.8 ± 5.52 pA (D1) and 44.17 ± 5.91 pA (D2), and the values were significantly different ($p < 0.001$). The mean values for the S2 sensor were 58.60 ± 8.25 pA (D1) and 86.05 ± 7.60 pA (D2), and these values were significantly different ($p < 0.001$). Thus the S1 sensor the signal from D1 was always higher than at D2, whereas for the S2 sensor, the signal at D2 was always higher than D1. Thus we report a precise, stable, and repeatable signal, along with a statistically significant difference between the detectors in each sensor for live mouse sensing.

3.3 Determination of Positional Effects Between Phantom and Sensor on Sensor Signal

We hypothesized that imperfect sensor positioning resulted in variation during the repeatability studies described above. To better understand effects of sensor positioning, we varied the distance between the sensor and tissue-simulating cylindrical phantom. As expected, we observed an exponential decrease in signal with distance in the sensor [Fig. 3(a)] with similar values of CV% at all heights tested (Table 4, CV %). Note that there is a large decrease in signal ($\sim 50\%$) between having the sensor in direct contact to only 5 mm above the phantom. Next we studied how the angle between the phantom and the sensor affects the signal. This may be important for live animal sensing, since it may be difficult to find the exact angle between sensor and animal without any variation between measurements. The sensor was placed perpendicular to and nearly in direct contact with the phantom, again at a distance of 100 μm . We varied the angle θ between phantom and horizontal, from 0 deg and 15 deg, at 5-deg increments [Fig. 3(b)], while keeping the sensor fixed vertically. We observed a nonlinear change in signal with respect to angle. For example, S1D1 changed 112%, while S1D2 changed 181%, when the angle was varied between 0 and 15 deg [Fig. 3(c)]. However, the precision remained <2.28% at all positions for both detectors (Table 5, CV %). Next we evaluated whether the signal depended on the rotational position of the sensor with respect to the object. With the sensor perpendicular to the phantom surface, we rotated the cylindrical-shaped phantom, and we observed no change in the signal. We then set an angle " θ " equal to 5 deg between the phantom and the horizontal and applied this angle at four different position numbers (1 to 4) separated by " φ " (incremented by 90 deg), in a counterclockwise fashion around the phantom [Fig. 3(d) to 3(e)]. This resulted in a dramatic signal change between each position number [Fig. 3(f), Table 6] for each detector. For example, the signal ranged from 18.2 pA in position 3 to 36.5 pA in position 4, or a 101% increase. However, the precision remained unaffected, ranging from <1.32% for D1 and <2.06% for D2 (Table 6, CV %). In summary, these data suggest that despite variation in signal in response to sensor positioning, precision does not change appreciably when increasing distance, or angle, or when rotating sensor with respect to the phantom. Additionally, our data suggests sensitivity to positions will likely be present during fluorescence sensing, emphasizing the need for stable sensor architecture.

Table 2 Repeatability of S1 and S2 sensors in open, phantom, and *in vivo* conditions for $N = 5$ (open and phantom) and $N = 14$ (*in vivo*) measurements.

Configuration	Mean-D1 (pA)	Stdev (pA)	Mean-D2 (pA)	Stdev (pA)	D1 CV%	D2 CV%
S1-open	11.478	2.948	5.984	2.088	25.684	34.897
S1-phantom	79.911	17.865	62.662	14.954	22.356	23.865
S1-mouse	75.814	5.522	44.172	5.9106	7.284	13.381
S2-open	6.758	1.797	10.329	1.800	26.587	17.426
S2-phantom	34.639	6.318	78.089	7.579	18.240	9.706
S2-mouse	58.598	8.247	86.053	7.596	14.074	8.827

Table 3 Long-term precision of signal as measured by coefficient variation of S1 sensor in open, phantom configurations ($N = 4$ trials).

#	D1			D2		
	Open CV%	Phantom CV%	Mouse CV%	Open CV%	Phantom CV%	Mouse CV%
1	1.166	1.979	2.180	2.825	3.290	3.271
2	0.715	0.729	0.652	1.114	1.002	2.385
3	3.311	2.366	1.306	2.338	2.071	1.391
4	0.640	1.708	1.807	1.211	2.519	1.690

Table 4 Precision of signal as measured by coefficient of variation for the S1 sensor due to change in distance between phantom and sensor.

Distance (cm)	S1D1			S1D2		
	Mean	Stdev	CV%	Mean	Stdev	CV%
0	66.882	0.534	0.798	49.310	0.642	1.301
0.5	32.907	0.436	1.325	24.581	0.529	2.154
1	17.428	0.132	0.758	12.899	0.101	0.779
2	10.313	0.075	0.723	6.841	0.079	1.151
3	7.965	0.077	0.972	4.448	0.092	2.067

Table 5 Precision of signal as measured by coefficient variation for the S1 sensor during change in angle between phantom and sensor.

Angle (deg)	D1			D2		
	Mean	Stdev	CV%	Mean	Stdev	CV%
0	31.802	0.095	0.298	21.259	0.097	0.455
5	39.684	0.420	1.059	26.009	0.501	1.928
10	37.427	0.438	1.181	19.597	0.440	2.277
15	57.531	0.163	0.283	40.908	0.218	0.532

3.4 Determination of Variation in Sensor Signal for In Vitro, Fluorescent Phantom, and Live Mouse Fluorescent Sensing

We performed *in vitro* experiments to determine repeatability between the two sensors in the presence of fluorescence. We varied the concentration between 250, 500, 2500, and 10,000 nM. With the sensor fixed below a clear well containing Cy5.5 dilutions, the S1 sensor output signal varied linearly with fluorophore concentration, as did the S2 sensor [Fig. 4(a), $N = 5$ measurements per concentration]. We compared the linearity and variation at each point with the S2 sensor and

Table 6 Precision of signal as measured by coefficient variation for the S1 sensor during rotation of 5-deg angle of phantom to horizontal at four different positions.

Position #	D1			D2		
	Mean	Stdev	CV%	Mean	Stdev	CV%
Control	50.905	0.322	0.633	31.291	0.178	0.570
1	24.900	0.114	0.459	15.958	0.092	0.579
2	33.845	0.447	1.321	22.863	0.403	1.765
3	18.150	0.239	1.315	11.371	0.235	2.067
4	36.531	0.453	1.239	24.852	0.401	1.612

observed similar results [Fig. 4(b)]. To compare variations between detectors for each sensor, we plotted the mean value of one detector versus the mean value of the other detector at each concentration [Fig. 4(c)]. The data demonstrates that between each sensor, the signals correlate linearly [Fig. 4(c), arrows], but not in a one-to-one fashion. This can be appreciated by comparing the line for S1 (blue) or S2 (red) to the line for “ $y = x$.” Because of the linear relationship between detector signal and concentration, it is possible to calibrate the two sensors, but for characterization studies we use only raw data from each sensor. Repeatability, as measured by a variation in signal after repeat measurements, ranged from $<0.92\%$ (250 nM), $<0.69\%$ (500 nM), $<6.77\%$ (2500 nM), and $<3.25\%$ (10,000 nM), and similar results were obtained with the D2 detector and with the S2 sensor.

We then wanted to determine repeatability in sensing of fluorescence in a phantom model. A glass capillary tube filled with 50 μM Cy5.5 was fixed inside a container of liquid phantom formulated with 0.6% intralipid in distilled water to model tissue scattering ($\mu'_s = 6 \text{ cm}^{-1}$ at 700 nm). The sensor was fixed and submerged in the container. The container, containing the capillary tube and liquid phantom material, was translated on a stage relative to the sensor. To avoid any effects of submersion, we engineered two similar sensors to S1 and S2, just for fluorescent phantom experiments. We used a liquid fluorescence-emitting phantom filled with the Cy5.5 fluorophore (50 μM) [Fig. 4(d)]. We measured the signal while keeping the sensor fixed and moving the container in the x or y (laterally) or z (axially) direction in relation to the sensor. As expected, variation in depth of fluorophore resulted in an exponential reduction in signal [Fig. 4(e)]. We first measured the repeatability with the fluorescence phantom, and the repeatability varied from less than 12.99% (CV% $N = 2$ trials, $N = 4$ detectors). We then normalized the data for each sensor, and, using this approach, the variation increases to 9.60% at the highest depth of 3.2 mm (CV%).

To further determine the source of potential error in movement and positioning, we determined the field of view of the sensor using the fluorescent phantom. We performed a two-dimensional (2-D) plot to determine lateral and depth resolution. Our data demonstrates the effect of lateral distance and height on signal [Fig. 4(f), $N = 2$ trials, $N = 4$ detectors]. At the center of the phantom ($y = 0$), the sensed signal from a volume of tissue containing fluorophore is a weighted average, with 90% of the

signal coming from the first 1.9 mm [Fig. 4(f)]. As expected, at greater depths, there is decreased lateral resolution, as expected due to multiple scattering events. Overall, our data can be used to estimate a field of view of approximately $2.5 \times 2.5 \times 2$ mm ($L \times W \times H$) for our studies.

To understand variation when detecting fluorescence in live mice, we injected different concentrations of fluorophore subcutaneously (directly underneath skin) and performed sensing, again with the S1 and S2 sensors used previously. A representative plot demonstrates the signal was stable for 600 s at a concentration of 500 nM [Fig. 4(g)]. We measured signal variation by calculating the CV% based on the variation with time. The signal typically varied within 5% of the mean, and both detectors behaved similarly.

3.5 Continuous Dynamic Sensing of the Intravenously Injected Fluorophore

A molecular probe is commonly administered intravenously, typically via the tail vein in a mouse, which results in the probe being subject to biodistribution via blood vessels and elimination via kidneys and or the liver, resulting in a tissue time-activity curve for a given tissue region of interest. Since we wanted to perform sensing of dynamics of molecular probe in the presence of tumors, we first wanted to establish dynamic of sensing a fluorophore (without a targeting moiety) in the absence of tumor. To establish dynamic sensing we first measured the background signal for ~ 1000 s, then injected 5 nmol of Cy5.5 intravenously in a live mouse and acquired data for at least 4000 additional seconds. Two sensors were used, placed bilaterally near the hindlimb. A typical time-activity curve consisted first of a constant, stable background signal, then a brief increase, and finally a slow decrease [Fig. 5(a)]. During all stages, the two detectors of each sensor exhibited identical dynamic changes. We performed baseline correction of each to further understand differences in kinetics between the two sensors. Interestingly, after baseline correction, we found that the signal peak reaches approximately the same level, but the S2 signal clearly decays at a higher rate [Fig. 5(b)]. For example, after 4000 s, the S1D1 signal is approximately 36 pA and the S2D1 signal is approximately 23 pA. Assuming that differences in scattering are accounted for by background subtraction, our data suggests that the fields of view illuminated by S1 and S2 sensors are heterogeneous with respect to fluorophore kinetics. We then plotted the raw kinetic data on a detector 1 versus detector 2 plot, and labeled the portions that correspond to dynamic portions of the curve in Fig. 5(a) in Fig. 5(c). The data was co-linear for both sensors over the entire time-activity curve. To demonstrate the co-linearity of the lines quantitatively, we performed linear curve fitting for each line [Fig. 5(c)]. The slope of the curve for the S2 curve was 0.989, while for the S1 curve was 0.979 [Fig. 5(c)], suggesting co-linearity. Our data validates that signal variation was likely due to change in fluorophore concentration and not due to change in the individual detector itself, which would result in a change in co-linearity on a detector 1 versus detector 2 plot.

To further understand how physiological variation in the living subject (mouse) affects signal, we performed controlled perturbation during sensing. Our preliminary experiments demonstrated that signal was extremely sensitive to small but abrupt changes in inhaled anesthesia (isoflurane) concentration. Since hemoglobin absorbs light at the VCSEL biosensor's excitation and emission wavelengths, we propose that the

change in signal could be due to isoflurane's known effects on vasomotor activity, blood flow, or neuromuscular-driven movement. After the mouse reached a steady state level of anesthesia based on breathing rate, we abruptly increased isoflurane concentration (by 25%) above the steady state level (typically 1% v/v). We performed this perturbation several times at equally spaced intervals (approximately 1000 s) [Fig. 5(d), labeled as "A" to represent changes in anesthesia]. Overall, there are five distinguishable segments of signal, which are numbered with arrows [Fig. 5(d)]. Each perturbation resulted in an abrupt change in signal that could be clearly observed. To understand whether the detectors behaved in a co-linear fashion, we plotted the data in each of these segments on a detector 1 versus detector 2 plot [Fig. 5(e)]. Even after perturbation, the data appears to be co-linear, as evidenced by the different color segments, which appear to follow the same slope, as shown with linear curve fits [Fig. 5(e)]. For example, the slope of segment 4 (red) was 0.714, while the slope of segment 3 was 0.774 (blue). This indicates that despite the change in signal for the sensor, the signal from both detectors changes coordinately. We conclude that our sensor captures the entire time-activity curve during continuous sensing. Additionally, our data suggests that changes in signal due to clearance of probe and dynamic changes during perturbation signal can be detected. In the presence of perturbation, the two detectors in each sensor continue to behave in a coordinate fashion. Last, we demonstrate that different sensors in different locations in the same mouse can demonstrate kinetic differences that signify heterogeneity between the two fields of view.

3.6 Quantitation of Continuous Sensing of the RAD-Cy5.5 and RGD-Cy5.5 Molecular Probes

Having established both precision and repeatability in the absence and presence of fluorophore, our goal was to noninvasively and continuously sense molecular probe in tumors. We chose the cRGD-Cy5.5 optical imaging probe and U87 tumor model, which are well-established molecular imaging probe and tumor models. We first chemically synthesized cRGD-Cy5.5 (RGD) [Fig. 6(a)] and the control, nontargeting probe, cRAD-Cy5.5 (RAD) and ensured the compounds were pure. We established that these probes function as expected using a small animal fluorescence imager with a cooled CCD camera. We injected tumor-bearing mice with 3 nmol of RAD ($N = 3$ mice) and RGD ($N = 3$ mice) via tail vein and imaged continuously for 2 h. As expected, fluorescence emission was greater in tumors of animals injected with RGD compared to RAD [Fig. 6(b), black arrows]. The mean tumor to background ratio (ratio of average radiance) from the tumor compared to the contralateral hindlimb (background) was significantly higher for RGD compared to RAD injected mice [Fig. 6(c), $p < 0.05$], validating the targeting of the RGD probe compared to the control RAD probe.

We then performed more experiments with the RAD and RGD probes in tumor-bearing mice using S1 and S2 sensors. To better understand the dual-sensing approach, we first analyzed the signal due to fluorescence by comparing the signal from S1D1 and S2D1 in a variety of fluorescence data sets. For all fluorescence data sets, we performed baseline correction. We determined that for *in vitro* dye studies at various concentrations (500 nM, 2.5 μ M, 10 μ M) the S2D1 to S1D1 ratio was 0.644 ± 0.02 . For all live mouse studies, the ratio was 0.652 and 0.589 at 2 h after injection of dye alone, in mouse #1 and mouse #2, respectively, for S2D1 to S1D1 ratio. When we injected

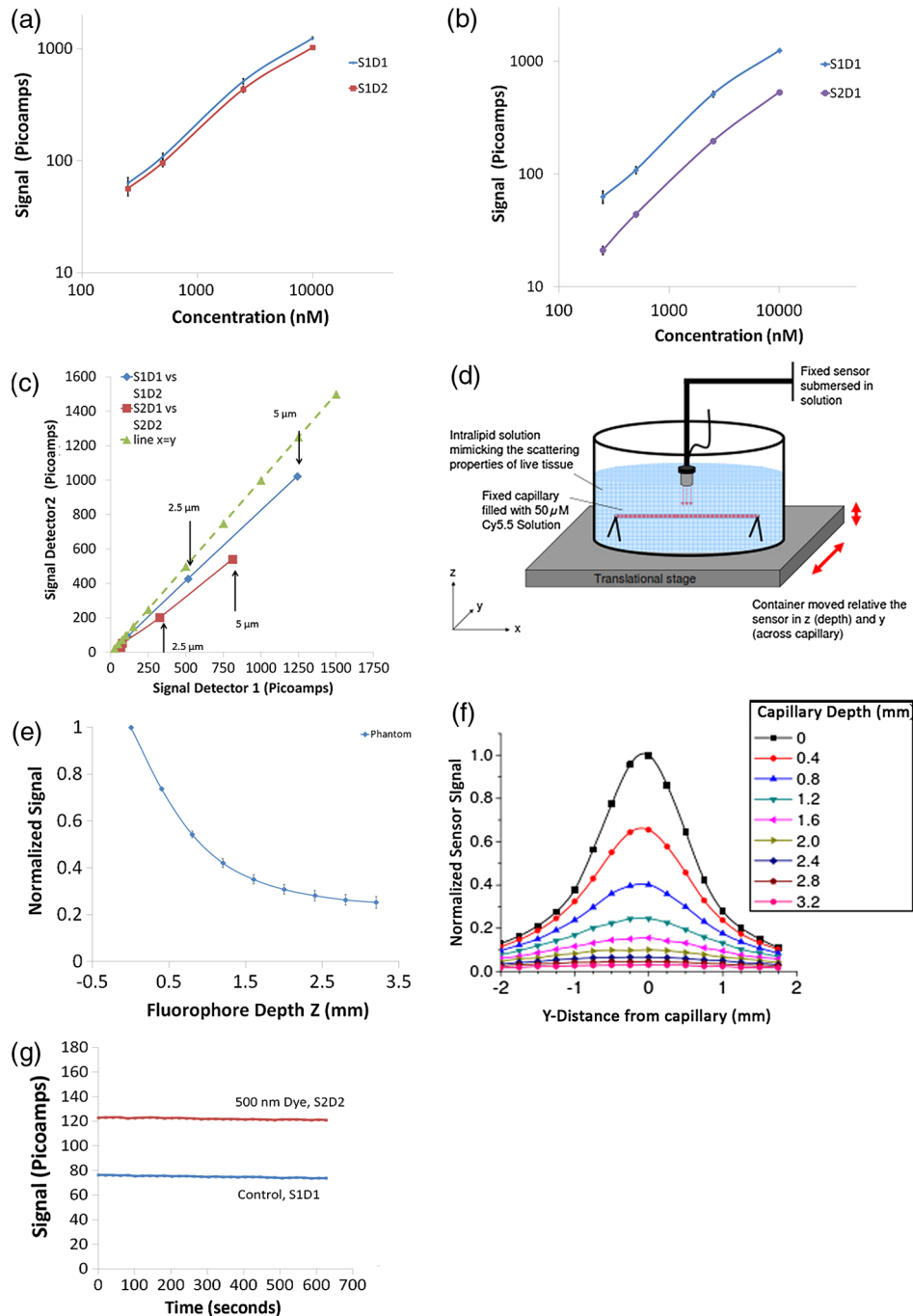


Fig. 4 Determination of effects of *in vitro*, phantom, and live mouse fluorescent sensing on sensor signal. (a) Plot of signal versus concentration of fluorophore for S1 sensors *in vitro*. Comparison is made between two detectors (D1 and D2) for the S1 sensor. 100 μl of Cy5.5 fluorophore is placed in one microwell of a standard 96 microwell plate, and sensor is placed vertically above the well at a distance of 2 mm. Ten measurements were made and averaged; this was repeated several times for each concentration and presented as mean of signal \pm standard deviation ($N = 6$). Four concentrations were tested here and data from both S1D1 and S1D2 is shown; (b) same data as in (a), except a plot of signal versus concentration of fluorophore for S1D1 and S2D1 detectors at each concentration; (c) same data as in (a), except a plot of the mean of the signal from detector 1 versus the mean of signal from detector 2 for S1 and S2 sensors, at each concentration. Two arrows point toward 2.5 mM (left) and 5.0 mM (right) for both the S1 sensor and S2 sensors. A plot of “ $y = x$ ” (dashed) is shown as a reference; (d) experimental system for fluorescence phantom sensing consisting of submerged functional sensor in a container containing 0.6% intralipid solution at room temperature. A fixed, sealed, capillary tube phantom containing 50- μM dye at base of container was used to mimic dye emitting object. Container was placed on a translational stage that could be moved controllably in the x, y, and z directions; (e) effects of distance from fluorescent phantom, on signal. Three experiments with a total of six detectors (two detectors per sensor) were performed. Mean and standard deviation was calculated at each depth. Signal was baseline corrected and normalized to maximum signal and averaged across all detectors; (f) effects of changes in lateral position of fluorescent phantom on signal. While keeping the depth constant, normalized signal was calculated at varying lateral distances from the capillary tube. Then depth is incremented and measurement is repeated. At zero capillary depth, the signal drops to 50% of normal at 0.75 mm lateral from the capillary, whereas at the 1.2 mm depth, the signal drop to 50% of the normal position at approximately 1.4 mm; and (g) plot of signal versus time for S1 and S2 sensor. Cy5.5 fluorophore at a concentration of 500 nM is injected subcutaneously on the right hindlimb of the mouse and detected by the S2 sensor. The S1 sensor is placed above the left hindlimb and no signal is detected.

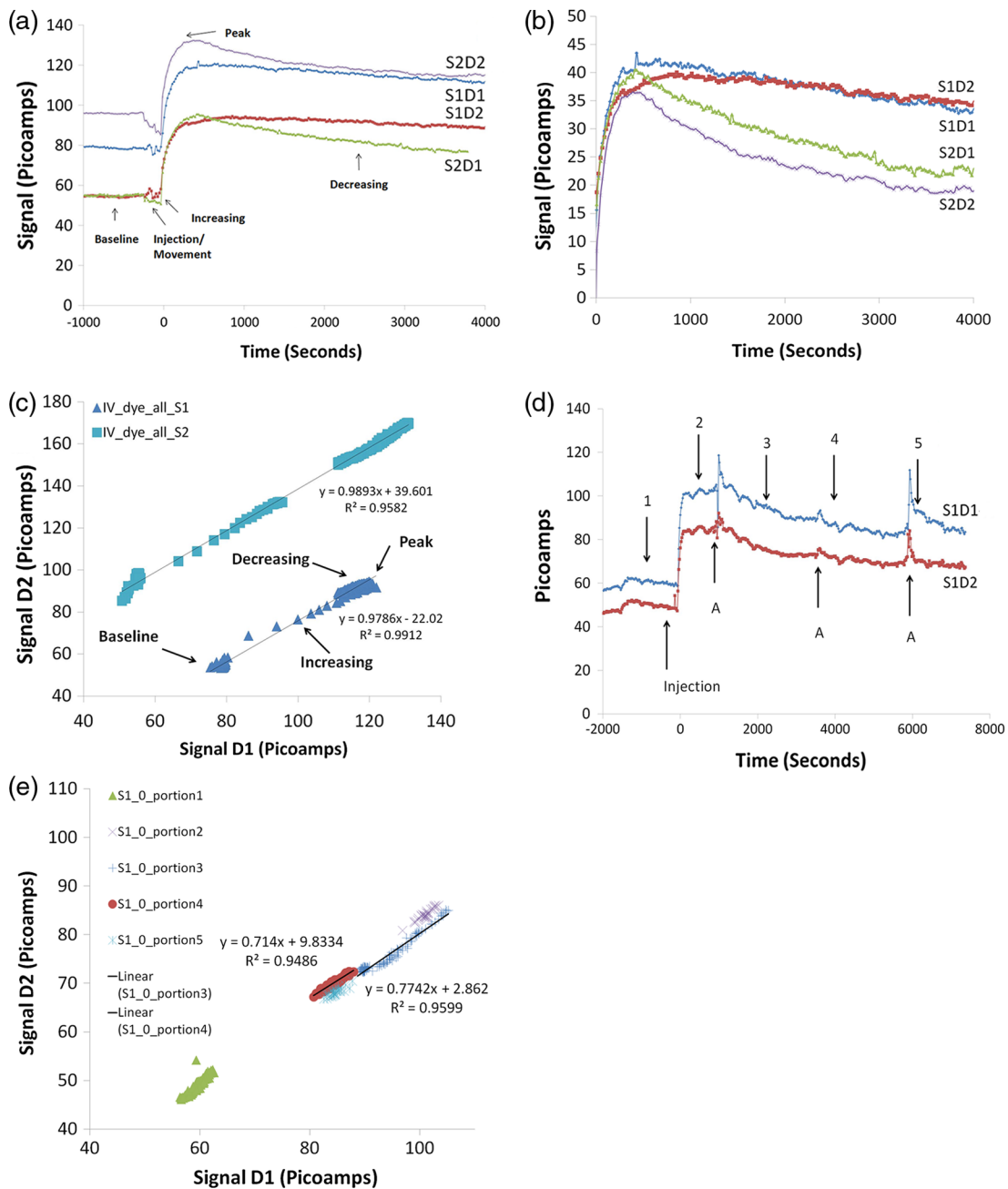


Fig. 5 Effects of intravenously injected fluorophore on sensor signal. (a) Plot of the signal from each sensor/detector combination versus time for a mouse injected with 5 nmol of Cy5.5 fluorophore intravenously via tail vein. Continuous data (every 20 s) acquired for approximately 1400 s prior to injection, and for a total of 4000 s, in an anesthetized nude mouse; (b) same data as in (a) except each curve has been baseline subtracted; (c) same data as in (a) except plot of the signal from detector D1 versus the signal of detector D2 for sensor S1 and for sensor S2. The labels correspond to those used in (a); (d) a plot of the signal for the S1 sensor for a mouse injected with 3 nmoles of Cy5.5 fluorophore intravenously, in which signal was perturbed by changing anesthesia during sensing, "A" at each point of perturbation. Five segments of each curve are labeled 1 to 5 and separated by points in which anesthesia, "A," was changed; and (e) same data as in (d) except plot of the signal from detector D1 versus the signal of detector D2 for sensor S1 and for sensor S2; the labels correspond to those used in (d).

tumor-bearing mice with the nontargeted RAD, which does not accumulate in tumors, we again calculated the S2D1 to S1D1 ratio. We plotted the averaged signal of S1D1 and S2D1, as well as the average ratio of these two [Fig. 6(d)]. The average S2D1 to S1D1 ratio after RAD injection was 0.542 ± 0.049 at 30 min, 0.523 ± 0.069 at 1 h, 0.476 ± 0.092 at 1.5 h, and 0.49 ± 0.113 at 2 h. In the RAD experiments, the tumor was on the S2 side in one of the mice and on the S1 side in two other mice.

Nevertheless, the ratio across several experimental systems was quite similar, and in all cases S2D1 was less than S1D1, and the ratio ranged from 0.476 to 0.542 for all RAD studies.

Next we evaluated the ratio of S2 (tumor side) to S1 (control side), after baseline correction, for tumor-bearing mice injected with RGD. The average S2D1 to S1D1 ratio after RGD injection was 1.236 ± 0.539 at 30 min, 1.254 ± 0.524 at 1 h, 1.362 ± 0.603 at 1.5 h, and 1.662 ± 0.75 at 2 h. We plotted

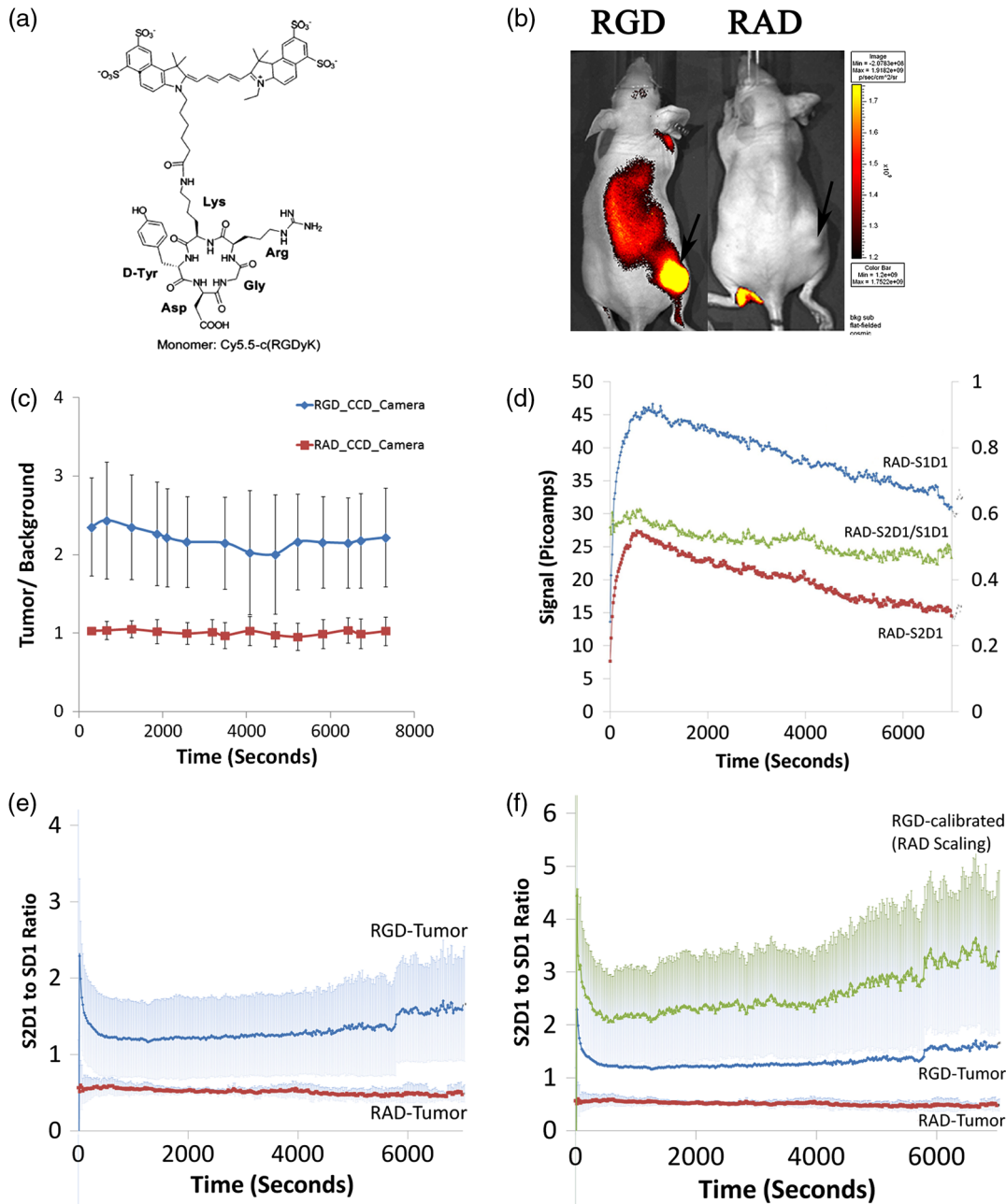


Fig. 6 Continuous sensing of the RAD-Cy5.5 and RGD-Cy5.5 molecular probes in tumor-bearing mice. (a) Chemical structure of c(RGDyK)-Cy5.5. The c(RADyK)-Cy5.5 has alanine(A) substituted instead of glycine(G); (b) representative image of nude mice bearing U87 tumor xenografts injected via tail vein with 3 nmol of cRGD-Cy5.5 ($N = 3$, left) or 3 nmol cRAD-Cy5.5 ($N = 3$, right) acquired using a cooled CCD camera. Mice were anesthetized, injected simultaneously, and sequentially imaged for 2 h. Emission was filtered using a Cy5.5 filter. Tumor is located on right hindlimb of each mouse (black arrow); (c) plot of signal-to-background ratio versus time for the same mice in (b) continuously imaged with cooled CCD camera. Quantification performed on images of cRGD-Cy5.5 injected ($N = 3$) and cRAD-Cy5.5 injected ($N = 3$) mice using average radiance (photons/sec/cm²/sr). Data presented as mean \pm deviation; (d) double plot of averaged RAD data for S1 and S2 sensors (left axis) and S2D1 to S1D1 ratio (right axis). Tumor-bearing mice ($N = 3$) were injected with the cRAD-Cy5.5 (nontargeted) probe and dual sensing was performed for 2 h. For mouse 1, the tumor was sensed by the S1 sensor; for mouse 2 and 3, the tumor was sensed by the S2 sensor; (e) plot of the averaged S2D1 to S1D1 ratio (mean \pm deviation) for tumor-bearing mice injected with the cRAD-Cy5.5 (control nontargeted, $N = 3$) probe and cRGD-Cy5.5 (targeted, $N = 5$) probe. Dual sensing was performed for 2 h; and (f) same as in (e), but averaged, calibrated S2D1 to S1D1 ratio is also shown in green. Calibration was performed by dividing averaged cRGD-Cy5.5 data by the averaged cRAD-Cy5.5 data.

the ratio for RAD and RGD injected mice together [Fig. 6(e), mean \pm S.D., $p < 0.05$]. We observed statistically significant differences at all time points, and the curves appeared nearly identical to the case of analysis using the cooled CCD camera. Finally, we wanted to perform a calibration. Our simplest approach was to scale the RGD data by dividing each point

by the RAD curve. This assumes that ratio of the two sensors for RAD injected mice should be 1, as we observed with images of our cooled CCD camera data. To normalize the RGD data to the RAD data, we performed a point-by-point division such that each point in the RGD ratio is divided by each point in the RAD ratio at each time. This resulted in a tumor-to-background

similar to the cooled CCD camera data as shown [Fig. 6(f)]. For the calibrated ratio, the average S2D1 to S1D1 ratio was 2.367 ± 1.029 at 0.5 h, 2.437 ± 0.950 at 1 h, 2.929 ± 1.274 at 1.5 h, and 3.640 ± 0.1379 at 2 h. This compares favorably with *in vivo* studies performed previously.³⁴

3.7 Kinetics of Molecular Probe in Individual Mice During Continuous Sensing of the RAD-Cy5.5 and RGD-Cy5.5 Molecular Probes

Since many biological processes are dynamic with varying time and length scales, the ability to assess signal kinetics, and perform continuous imaging in each field of view has important

implications for assessing functional differences of molecular probes. By using a dual-sensing strategy, we obtained quantitative information of the fluorescent molecular probe. Normally, after probe injection, dynamic signal from a single sensor was similar [Fig. 7(a)], with different magnitudes. We normalized the signal and compared signal after RAD injection from the same S1D1 detector across different mice. A wide range of signal dynamics was present between the same RAD probe across different mice [Fig. 7(b), $N = 3$]. Furthermore, we compared the kinetics of RGD probe in mice bearing U87 tumors. Interestingly, we again observed a wide range of decay kinetics over 2 h, ranging from approximately 90% to 30% of initial signal, 2 h after injection [Fig. 7(c), $N = 5$, $N = 3$ shown]. Last, we

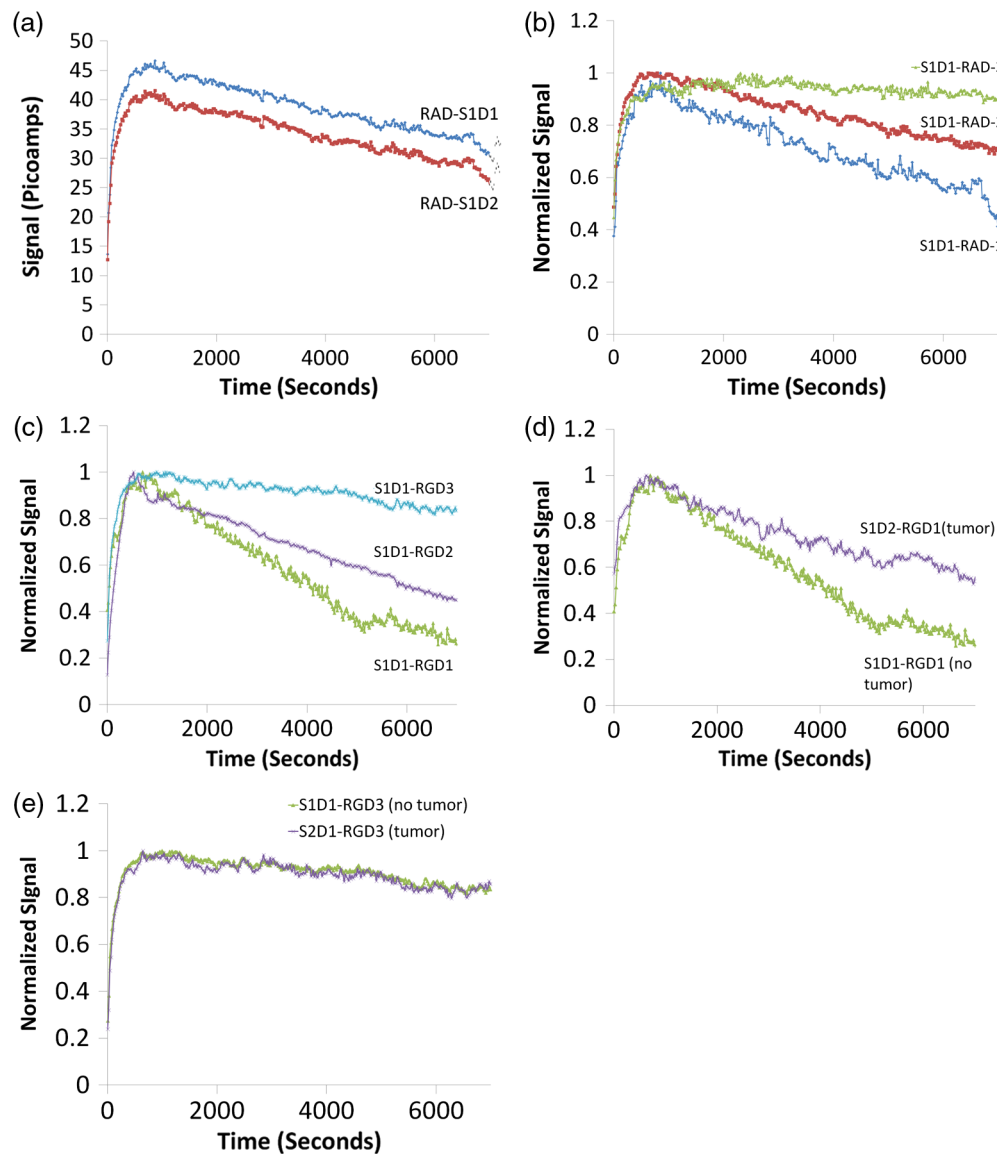


Fig. 7 Kinetics of molecular probe in individual mice during continuous sensing of the RAD-Cy5.5 and RGD-Cy5.5 molecular probes. (a) Representative, baseline-corrected raw data plot of sensor signal versus time for S1D1 and S2D2 in nude mice bearing U87 tumor xenografts injected via tail vein with 3 nmol of cRAD-Cy5.5; (b) baseline-corrected, normalized data plot of sensor signal versus time for S1D1 for three individual nude mice bearing U87 tumor xenografts injected via tail vein with 3 nmol of cRAD-Cy5.5; (c) baseline-corrected, normalized data plot of sensor signal versus time for S2D1 in individual nude mice bearing U87 tumor xenografts injected via tail vein with 3 nmol of cRGD-Cy5.5. S2 was sensing tumor in mouse 1, and S1 was sensing tumor in mouse 2 and 3; (d) baseline-corrected, normalized data plot of sensor signal versus time for S1D1 and S2D1 for individual nude mice bearing U87 tumor xenografts injected via tail vein with 3 nmol of cRGD-Cy5.5. Same as mouse #1 from (c); and (e) baseline-corrected, normalized data plot of sensor signal versus time for S1D1 and S2D1 for individual nude mice bearing U87 tumor xenografts injected via tail-vein with 3 nmol of cRGD-Cy5.5. Same as mouse #3 from (c).

compared the signal kinetics between tumor and normal tissue in an individual mouse, after injection of RGD. In both cases, the signal to background ratio was greater than 2, when we examined the absolute signal. Surprisingly, we found two different kinetic patterns. In one case, the RGD signal was decreasing faster in the normal tissue than the tumor [Fig. 7(d)], reaching approximately 60% and 30% of initial signal, respectively. In another case, the RGD signal decreased at the same rate in normal and tumor tissue and was approximately 85% after 2 h [Fig. 7(e)]. Our data demonstrates that the VCSEL-biosensor can also be used to study normalized data. Thus, the relative difference in kinetics of molecular probes in mice can be quantitatively measured. Using this approach, we measured differences between mice, between probes, and between tissue types (tumor versus normal).

4 Discussion

In this study, we develop, for the first time, a novel optical sensor and sensing strategy for performing noninvasive molecular sensing of a molecular imaging probe in live animals. We demonstrate a precise sensor for live mouse sensing and analyze variability under conditions of both backscattered and fluorescent light. We use tissue and fluorescent phantoms to understand effects of distance, angle, and field of view. The VCSEL biosensors stay reliably precise during these studies, with both detectors in each sensor, and two distinct sensors behaving near-equivalently. We also demonstrate fluorescent sensing in several live mouse models, including subcutaneous dye, injected fluorophore, and targeted and nontargeted fluorescent molecular probes. In these studies, our sensor fully captures the time-activity curves and demonstrates heterogeneity in signal between two fields of view in two different sensors. We then perform dual sensing in a cancer model using the established $\alpha_V\beta_3$ integrin targeted (cRGD-Cy5.5) and nontargeted (cRAD-Cy5.5) fluorescent molecular probes. We demonstrate nearly identical tumor to background levels between a conventional cooled CCD camera and the VCSEL biosensor. Last, we demonstrate the ability to quantitatively capture differences in probe kinetics between different mice using the same sensor.

Our approach to determining the suitability of the VCSEL biosensor for live mouse sensing was to analyze sources of variability and to determine the relative importance of these sources. Our data suggests that once the sensor is fixed in a particular location, the sensor is precise, but when the sensor is repeatedly repositioned, then larger variation occurs. Another cause of variability is the angle between the sensor and the living subject (5 to 15 deg) and observed large changes in magnitude of signal (180%) without changes in precision. Furthermore, fixing the angle of the phantom at 5 deg (θ), with respect to the sensor, and rotating the phantom at a second angle (φ) caused a large change in magnitude of the signal (200%). This suggests that despite careful attention to the fluorescence emission filter on the detector,¹⁹ excitation light still leaks to the detector, especially at higher angles of incidence. This is consistent with our sensor design, since the detector is partly based on an interference filter, which has an angular dependence of transmission. The sensor also appears to have a rotationally dependent field of view. This is expected since the VCSEL sources are placed on the optical axis of the lens, while the detectors sit off-axis. Some ways to address this in future designs of the sensor might be to adapt an integrated design with rotational symmetry.²⁰ Another approach is to incorporate positional sensing

into the device itself. This might help avoid any unknown positional changes of the sensor during long-term sensing in one subject. We expect our next-generation devices to have improved positional sensitivity.

A critical point of our studies was the consistent difference in responsivity between sensors during fluorescent sensing. Surprisingly, we found the same differences in responsivity across several experimental systems, including *in vitro* live mouse with injected dye only and live mouse probe experiments with nontargeted injected probe. Nevertheless, we used nontargeted (RAD) probe to calibrate our data with the targeted (RGD) probe, resulting in nearly identical time-activity curves to the ones obtained from the cooled CCD camera. One limitation with this approach is that we tested only one concentration of both nontargeted and targeted probe and not several concentrations. However, in terms of responsivity differences, our *in vitro* studies demonstrate that at several concentrations, the responsivity was unchanged. A second limitation is that in our experiments with nontargeted probe, we measured responsivity only when sensing a tumor on one side, not both sides. Nevertheless, we observed only a small variation in the ratio across multiple mice. Overall, our data suggests that once signal is baseline corrected, the internal characteristics of the sensor dominate over external characteristics such as positioning. Because there is an inherent problem with quantifying absolute fluorophore concentration without first determining the underlying optical properties of the tissue (for any diffuse fluorescence technique), the sensor is best suited for measuring relative changes and dynamics, which we have performed in this study. Future work will be performed to understand differences in responsivity in the sensor during sensor design, different *in vivo* concentrations, how tumors may affect measurements of *in vivo* responsivity, and new approaches to calibrating differences in responsivity.

An important advantage of our VCSEL biosensor is the ability to directly obtain a direct kinetic readout of a time-activity curve within a particular field of view. Kinetics is a critical design parameter for molecular probes targeting specific receptor systems. Analysis of the kinetics of molecular probes using an optical signal, while not as accurate as a whole body tomographic technique like positron emission tomography (PET), still can give a semi-quantitative understanding of receptor ligand affinity, receptor expression levels, and receptor turnover levels. Ideally, one could use compartmental modeling to understand how signal relates to the complex process of transport of probe from blood, through the interstitium, to a biological target of interest, which itself has varying amounts of receptor number, affinity of binding, receptor recycling, and biological function. This approach has been taken using conventional optical imaging data.³⁸⁻⁴⁰ The importance of kinetics of probes has also been highlighted by optically segmenting internal organs based on differences in their kinetic properties.⁴¹ In our study, differences in kinetics were present after injection of RGD peptide in two tumor-bearing mice, both of which have an increased tumor to background ratio (1.5 to 3). Interestingly, one mouse demonstrates similar kinetics of signal decay between the tumor and background (Fig. 7), while the other demonstrates that signal decay is decreased in tumor compared to the control site. This suggests that two different kinetic mechanisms may exist, both of which give rise to an increased signal-to-background ratio. To our knowledge, these types of differences have not been previously reported. We believe

these differences are due to tumor heterogeneity, an important aspect of tumor biology, which our sensor can directly address. Ideally, there would be the same amount of target, exposed to the same concentration of molecular probe in all cases. In our case, we arbitrarily placed our sensor in the center of the tumor in the exact same orientation in all experiments. However, because of the large field-of-view of the device, and since the tumor was visible from the skin surface, we are confident that we accurately sampled the tumor volume. Future work with detailed pharmacokinetic analysis and additional mice should shed light on different properties of tumors and what factors give rise to differences in kinetics.

Our study highlights the robustness of the fluorescence component of the VCSEL biosensor, including the detector, laser, and optical filters. This is evidenced by linearity of signal *in vitro* and *in vivo*. Furthermore, the VCSEL biosensor demonstrates flexibility across a wide range of sensing platforms, and demonstrates repeatability and long-term stability. Last, the VCSEL biosensor is comparable to the cooled CCD camera for detecting relative levels of a molecular probe within a tumor compared to a nontargeted probe. We are currently designing VCSEL implantable biosensor systems that can be used to interrogate internal tissues and not just externalized tissue.²¹ Within our aim to eventually design VCSEL biosensors that operate in freely moving mice, we feel that the fluorescent component of the implanted sensor has now been optimized. To transition to implantable systems, we can now turn our attention to several other design improvements. A key improvement would be to fix the orientation of the sensor and to prevent unwanted gross and fine movement that would occur in a freely moving subject. Some possibilities could be to use more lightweight materials to house the sensor, to develop mechanical approaches to dampen movement, to develop algorithms that can correct signal for motion artifact, or to remotely measure and control the actual position of the sensor. Despite its near-infrared excitation capabilities, in its current design the VCSEL biosensor would have to be placed in direct proximity to the tissue of interest. Three cardiovascular examples that may offer clinical benefit include detecting fluorescent circulating endothelial progenitor cells, detecting a molecular probe, which targets a vulnerable atherosclerotic plaque in a large artery or vein, and detecting a molecular probe, which monitors acute thrombosis within an artery. Neurological applications in chronic disease monitoring, such as Alzheimer's or Parkinson's disease, for which molecular probes exist, and for which chronic therapeutic monitoring might be performed. Cancer, which requires therapeutic monitoring of a molecular target after treatment, or extravasation of fluorescent tumor cells on the edge of a solid tumor, would be another important clinical application. Monitoring implanted stem cells that express a near-infrared fluorescent protein in order to understand dormancy and eventual proliferation of these cells and their progeny would also be an important application.

Overall, we have created a miniature fluorescent VCSEL biosensor, and performed detailed characterization studies establishing its precision and how it senses the tumor using a probe targeted for $\alpha_V\beta_3$ integrin. Now that the fluorescent-sensing component of the VCSEL biosensor has been optimized, new design improvements can be implemented. These VCSEL biosensors could have utility pre-clinically and clinically for both noninvasive and invasive fluorescent molecular sensing. They can be potentially used in a wide range of clinical

settings, such as critical care settings, operating rooms, routine medical examination rooms, and home use, particularly with the cardiovascular, neurological, and cancer applications mentioned above. The devices could be used either noninvasively or minimally invasively, either as standalone devices or integrated into existing diagnostic or therapeutic medical devices. We anticipate expanded opportunities for VCSEL biosensing in freely moving animal subjects and eventually in patients.

Acknowledgments

The authors are grateful for the helpful discussions and assistance during experiments with Zachary Walls during the early phases of this project. The authors want to thank Anthony Kim (Ontario Cancer Institute–Princess Margaret Hospital). The authors also wish to thank Mary Hibbs-Brenner and Klein Johnson from Vixar, Inc. for assistance in epitaxial growth; Choma Technology Corp. for its generous donation of emission filter coatings; and Brealut Research Organization for an educational license of ASAP. We thank Brian Wilson, of Princess Margaret Hospital, and Elizabeth Monroe, of University of Toronto, for making the tissue phantom and measuring its properties. Fabrication of devices was carried out in the Stanford Nanofabrication Facility (SNF). This work was supported in part through an Interdisciplinary Translational Research Program (ITRP) grant through the Stanford University Beckman Center for Molecular and Genetic Medicine (SSG & JSH) and from the National Cancer Institute ICMIC P50 CA114747 (SSG). It is also supported in part through the University of Toronto departmental start-up funds to OL, the Natural Sciences and Engineering Research Council of Canada (NSERC) Discovery Grant RGPIN-355623-08 and by the Networks of Centres of Excellence of Canada, Canadian Institute for Photonic Innovations (CIPI). Funding for materials was provided through the Photonics Technology Access Program (PTAP) sponsored by NSF and DARPA-MTO. NP was supported by NIH T32 Training grant and Stanford Dean's Fellowship. TDO acknowledges graduate support from a National Defense Science and Engineering Graduate (NDSEG) fellowship, the U.S. Department of Homeland Security, and an SPIE scholarship. Dr. S. Cho is supported by the National Research Foundation of Korea Grant funded by the Korean government [NRF-2011-357-D00155].

References

1. M. L. James and S. S. Gambhir, "A molecular imaging primer: modalities, imaging agents, and applications," *Physiol. Rev.* **92**(2), 897–965 (2012).
2. A. Quon and S. S. Gambhir, "FDG-PET and beyond: molecular breast cancer imaging," *J. Clin. Oncol.* **23**(8), 1664–1673 (2005).
3. J. K. Willmann et al., "Molecular imaging in drug development," *Nat. Rev. Drug Discov.* **7**(7), 591–607 (2008).
4. M. A. Pysz, S. S. Gambhir, and J. K. Willmann, "Molecular imaging: current status and emerging strategies," *Clin. Radiol.* **65**(7), 500–516 (2010).
5. Y. A. Cao et al., "Shifting foci of hematopoiesis during reconstitution from single stem cells," *Proc. Natl. Acad. Sci. U.S.A.* **101**(1), 221–226 (2004).
6. F. Cao et al., "In vivo visualization of embryonic stem cell survival, proliferation, and migration after cardiac delivery," *Circulation* **113**(7), 1005–1014 (2006).
7. P. R. Contag, "Bioluminescence imaging to evaluate infections and host response *in vivo*," *Methods Mol. Biol.* **415**, 101–118 (2008).
8. F. A. Jaffer et al., "Two-dimensional intravascular near-infrared fluorescence molecular imaging of inflammation in atherosclerosis and stent-induced vascular injury," *J. Am. Coll. Cardiol.* **57**(25), 2516–2526 (2011).

9. D. J. Hall et al., "Dynamic optical imaging of metabolic and NADPH oxidase-derived superoxide in live mouse brain using fluorescence lifetime unmixing," *J. Cereb. Blood Flow Metab.* **32**(1), 23–32 (2011).
10. R. K. Jain, "Normalization of tumor vasculature: an emerging concept in antiangiogenic therapy," *Science* **307**(5706), 58–62 (2005).
11. G. S. Filonov et al., "Bright and stable near-infrared fluorescent protein for *in vivo* imaging," *Nat. Biotechnol.* **29**(8), 757–761 (2011).
12. S. A. Hilderbrand and R. Weissleder, "Near-infrared fluorescence: application to *in vivo* molecular imaging," *Curr. Opin. Chem. Biol.* **14**(1), 71–79 (2010).
13. B. Barat et al., "Cys-diabody quantum dot conjugates (immunoQdots) for cancer marker detection," *Bioconjug. Chem.* **20**(8), 1474–1481 (2009).
14. J. V. Jokerst and S. S. Gambhir, "Molecular imaging with theranostic nanoparticles," *Acc. Chem. Res.* **44**(10), 1050–1060 (2011).
15. A. Nakajima et al., "CMOS image sensor integrated with micro-LED and multielectrode arrays for the patterned photostimulation and multi-channel recording of neuronal tissue," *Opt. Express* **20**(6), 6097–6108 (2012).
16. D. C. Ng et al., "Integrated *in vivo* neural imaging and interface CMOS devices: design, packaging, and implementation," *J. Sensors IEEE* **8**(1), 121–130 (2008).
17. M. Beiderman et al., "A low-light CMOS contact imager with an emission filter for biosensing applications," *IEEE Trans. Biomed. Circ. Syst.* **2**(3), 193–203 (2008).
18. B. A. Flusberg et al., "High-speed, miniaturized fluorescence microscopy in freely moving mice," *Nat. Methods* **5**(11), 935–938 (2008).
19. T. O'Sullivan et al., "Implantable semiconductor biosensor for continuous *in vivo* sensing of far-red fluorescent molecules," *Opt. Express* **18**(12), 12513–12525 (2010).
20. E. Thush et al., "Integrated bio-fluorescence sensor," *J. Chomatogr. A* **1013**(1–2), 103–110 (2003).
21. R. Heitz et al., "A low noise current readout architecture for fluorescence detection in living subjects," *ISSCC* pp. 308–310 (2011).
22. N. Ferrara and R. S. Kerbel, "Angiogenesis as a therapeutic target," *Nature* **438**(7070), 967–974 (2005).
23. R. K. Jain, "Antiangiogenic therapy for cancer: current and emerging concepts," *Oncology (Williston Park)* **19**(4 Suppl. 3), 7–16 (2005).
24. W. Cai and X. Chen, "Multimodality molecular imaging of tumor angiogenesis," *J. Nucl. Med.* **49**(Suppl. 2), 113S–128S (2008).
25. M. Eisenblatter et al., "Optical techniques for the molecular imaging of angiogenesis," *Eur. J. Nucl. Med. Mol. Imaging* **37**(Suppl. 1), S127–S137 (2010).
26. Z. Cheng et al., "Near-infrared fluorescent RGD peptides for optical imaging of integrin $\alpha_v\beta_3$ expression in living mice," *Bioconjug. Chem.* **16**(6), 1433–1441 (2005).
27. Y. Wu et al., "MicroPET imaging of glioma integrin $\alpha_v\beta_3$ expression using (64)Cu-labeled tetrameric RGD peptide," *J. Nucl. Med.* **46**(10), 1707–1718 (2005).
28. I. Dijkgraaf, A. J. Beer, and H. J. Wester, "Application of RGD-containing peptides as imaging probes for alphavbeta3 expression," *Front. Biosci.* **14**, 887–899 (2009).
29. I. Laitinen et al., "Evaluation of alphavbeta3 integrin-targeted positron emission tomography tracer 18F-galacto-RGD for imaging of vascular inflammation in atherosclerotic mice," *Circ. Cardiovasc. Imaging* **2**(4), 331–338 (2009).
30. X. Chen et al., "MicroPET and autoradiographic imaging of breast cancer alpha v-integrin expression using 18F- and 64Cu-labeled RGD peptide," *Bioconjug. Chem.* **15**(1), 41–49 (2004).
31. A. P. Pathak, M. F. Penet, and Z. M. Bhujwala, "MR molecular imaging of tumor vasculature and vascular targets," *Adv. Genet.* **69**, 1–30 (2010).
32. D. B. Ellegala et al., "Imaging tumor angiogenesis with contrast ultrasound and microbubbles targeted to $\alpha_v\beta_3$," *Circulation* **108**(3), 336–341 (2003).
33. J. E. Mathejczyk et al., "Spectroscopically well-characterized RGD optical probe as a prerequisite for lifetime-gated tumor imaging," *Mol. Imaging* **10**(6), 469–480 (2011).
34. X. Chen, P. S. Conti, and R. A. Moats, "In vivo near-infrared fluorescence imaging of integrin alphavbeta3 in brain tumor xenografts," *Cancer Res.* **64**(21), 8009–8014 (2004).
35. T. D. O'Sullivan et al., "Implantable optical biosensor for *in vivo* molecular imaging," *Proc. SPIE* **7173**, 717309(2009).
36. S. B. Ozkan et al., "The effect of Septrafilm on adhesions in strabismus surgery—an experimental study," *J. AAPOS* **8**(1), 46–49 (2004).
37. V. Ntziachistos et al., "In vivo tomographic imaging of near-infrared fluorescent probes," *Mol. Imaging* **1**(2), 82–88 (2002).
38. M. Gurfinkel et al., "Quantifying molecular specificity of $\alpha_v\beta_3$ integrin-targeted optical contrast agents with dynamic optical imaging," *J. Biomed. Opt.* **10**(3), 034019 (2005).
39. S. Kwon et al., "Imaging dose-dependent pharmacokinetics of an RGD-fluorescent dye conjugate targeted to $\alpha_v\beta_3$ receptor expressed in Kaposi's sarcoma," *Mol. Imaging* **4**(2), 75–87 (2005).
40. K. S. Samkoe et al., "High vascular delivery of EGF, but low receptor binding rate is observed in AsPC-1 tumors as compared to normal pancreas," *Mol. Imaging Biol.* **14**(4), 472–479 (2011).
41. E. M. Hillman and A. Moore, "All-optical anatomical co-registration for molecular imaging of small animals using dynamic contrast," *Nat. Photonics* **1**(9), 526–530 (2007).